NANO LETTERS

pubs.acs.org/NanoLett

Letter

In Situ Cryogenic HAADF-STEM Observation of Spontaneous Transition of Ferroelectric Polarization Domain Structures at Low Temperatures

Junsik Mun, Wei Peng, Chang Jae Roh, Sangmin Lee, Syo Matsumura, Jong Seok Lee, Tae Won Noh, and Miyoung Kim*

Cite This: *Nano Lett.* 2021, 21, 8679–8686

Read Online

ACCESS | Metrics & More | Article Recommendations | Supporting Information

ABSTRACT: Precise determination of atomic structures in ferroelectric thin films and their evolution with temperature is crucial for fundamental study and design of functional materials. However, this has been impeded by the lack of techniques applicable to a thin-film geometry. Here we use cryogenic scanning transmission electron microscopy (STEM) to observe the atomic structure of a $BaTiO_3$ film on a (111)-$SrTiO_3$ substrate under varying temperatures. Our study explicitly proves a structure transition from a complex polymorphic nanodomain configuration at room temperature transitioning to a homogeneous ground-state rhombohedral structure of $BaTiO_3$ below ~250 K, which was predicted by phase-field simulation. More importantly, another unexpected transition is revealed, a transition to complex nanodomains below ~105 K caused by an altered mechanical boundary condition due to the antiferrodistortive phase transition of the $SrTiO_3$ substrate. This study demonstrates the power of cryogenic STEM in elucidating structure−property relationships in numerous functional materials at low temperatures.

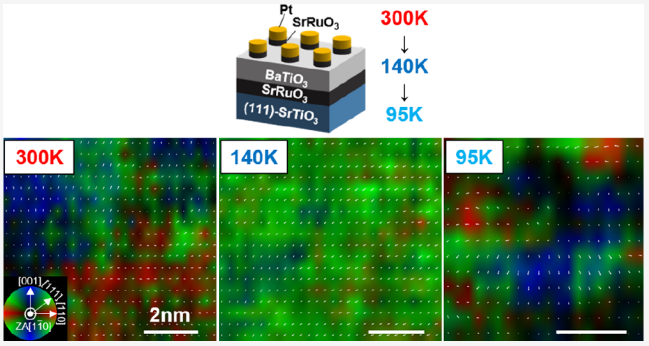

KEYWORDS: *in situ cryogenic STEM, phase transition, ferroelectrics, ferroelectric domain structures, epitaxial oxide films*

Ferroelectric materials exhibit spontaneous electric polarization, which can be switched between energy-degenerate states by applying electrical fields and/or mechanical forces.[1,2] This feature has been exploited in a variety of applications including memory devices, dielectric capacitors, and electromechanical units. Polarization switching is closely associated with domain configuration and crystal structure. The most important ferroelectric phenomena are spontaneous phase transition and the formation of polarization domains. The domain configurations and structural phases of ferroelectric film systems are strongly influenced by complex interactions associated with mechanical and electrostatic boundary conditions. This offers an opportunity to produce novel domain structures with promising device applications. For example, by exploiting misfit strain and epitaxial symmetry, researchers constructed morphotropic phase boundaries in single-compound oxide films.[3−5] Additionally, they observed polymorphic nanodomain structures,[6] similar to those discovered in chemically complex, high-performance piezoelectric ceramics. These complex nanoscale domains with varying structures and symmetries can provide a low-energy barrier for polarization rotation, which accounts for their extraordinary dielectric and piezoelectric responses.[7,8] For a better understanding and efficient implementation, it is important to obtain in-depth knowledge of the energetics of different structural phases and the evolution of domain structures under varying external forces or thermodynamic stimuli.

In recent decades, numerous experimental techniques have been developed for studying the domain configurations and local structures of ferroelectric materials. Among them, spherical aberration-corrected scanning transmission electron microscopy (STEM), particularly with in situ capabilities, is a powerful tool for atomic-scale analysis of ferroelectrics, such as nanoscale domain structures and atomic defects.[9−11] The advanced functionalities of in situ STEM allow the acquisition of real-time nanoscale images of domain switching,[12,13] domain growth,[14] and topological transformation of the domain structures,[15,16] and have thereby significantly enhanced our understanding of the energetics of complex domain structures,

Received: July 13, 2021
Revised: October 7, 2021
Published: October 13, 2021

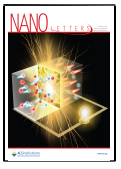

https://doi.org/10.1021/acs.nanolett.1c02729
Nano Lett. 2021, 21, 8679–8686

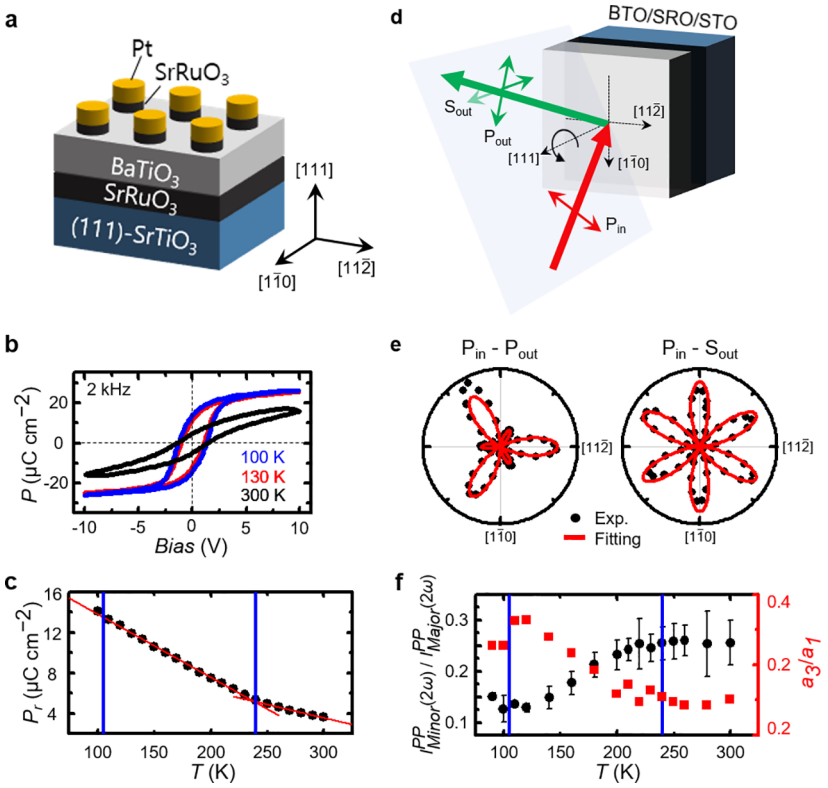

Figure 1. (a) Electrical measurement device. (b) Polarization−electric field (P−E) hysteresis loop measured at 300 K (black), 130 K (red), and 100 K (blue). (c) Plot of remnant polarization obtained by lowering the temperature from 300 to 100 K in increments of 10 K. Two solid red lines linearly fitted to two separate regions based on 240 K intuitively show the trend change by lowering the temperature. (d) Schematic diagram of the experimental setup for obtaining SHG signals. (e) Azimuth-dependent PP and PS SHG signal intensity of (111)-BTO measured at 300 K (black dots). Experimental SHG anisotropy patterns were fitted with C_{3v} point group symmetry (red solid lines). (f) Plots of the temperature- and azimuth-dependent $I^{PP}_{Minor}(2\omega)/I^{PP}_{Major}(2\omega)$ (black) and a_3/a_1 (red) of SHG signals, obtained by lowering the temperature from 300 to 90 K in 20 K increments and especially in 10 K increments around the transition temperature. (c, f) Two-stage phase transition temperatures under discussion are denoted by blue vertical lines, obtained based on second-order derivation.

leading to the optimization of ferroelectric domain engineering strategies.

However, STEM with in situ temperature control has rarely been used for obtaining atomic-scale information on domain and crystal structures near phase transitions. Previous low-temperature TEM studies have investigated the phase transitions of bulk $SrTiO_3$ (STO),[17] thiospinel $CuIr_2S_4$,[18] and bulk $BaTiO_3$ (BTO).[19] However, these studies were achieved mostly by using electron diffraction and probing a large area. This is due mainly to instability during scanning, arising from thermal drift caused by different thermal expansion coefficients among stages and/or target materials, and the vibration from bubbling of liquid nitrogen (LN_2) (Figure S1). These issues have been major barriers to the acquisition of reliable, high-quality atomic-resolution STEM images. Postprocessing techniques have been applied to overcome these issues.[20−25] Among these, image registration has been applied to obtain atomic-level STEM images to achieve picometer precision at low temperatures.[25] This method has successfully provided a way to clarify atomic arrangements at low temperatures using STEM, for example, charge-ordered Manganite[26,27] and 1T′-$TaTe_2$.[28] However, despite developments in methodologies and experimental techniques, ferroelectric nanodomain structures have not yet been investigated at atomic resolution under varying temperatures.

BTO is a displacive ferroelectric material with several structural phases: cubic, tetragonal, orthorhombic, and rhombohedral (from high to low temperature).[29−32] BTO changes the off-center direction of the Ti cation in each structural phase.[31] The tetragonal structure stabilizes at approximately room temperature, with the Ti cation being displaced from the center of the oxygen octahedron in the [001] direction. The orthorhombic and rhombohedral phases emerge at lower temperature with Ti displacing toward [110] and [111], respectively (Figure S2).

In this study, we applied cryogenic STEM to directly visualize the domain evolution in a (111)-BTO film at low temperatures. We mapped the displacement vectors of Ti cations with respect to the Ba cation cage as widely used[33−35] to observe the polymorphic nanodomains of the (111)-BTO film at room temperature,[6] and then cooled it to 140 K to further observe the development of a long-range polar order with a rhombohedral phase. The findings of this study demonstrate the critical role of epitaxial symmetry in the interaction between substrate clamping and domain formation in ferroelectric epitaxial films, highlighting the potential of cryogenic STEM for resolving long-standing issues pertaining to spontaneous phase transitions in material systems with complex nanoscale structures, such as relaxor ferroelectrics.[36]

We previously demonstrated that a 3-fold rotational symmetry enforced by a (111)-STO substrate on a BTO epitaxial film can induce a polymorphic nanodomain state (in

https://doi.org/10.1021/acs.nanolett.1c02729
Nano Lett. 2021, 21, 8679−8686

which the domain size ranged from 1 to 10 nm) with coexisting tetragonal, orthorhombiclike, and rhombohedral structures at room temperature.[6] Moreover, the polymorphic nanodomain state exhibits exceptional dielectric and piezoelectric responses, which are particularly intriguing for on-chip devices based on chemically simple ferroelectric thin films. According to our earlier phase-field simulations, we ascribed the enhanced properties to an electric-field-driven structural transition of polymorphic domains to a pure rhombohedral structure.[6,37,38] Notably, field-driven structure transitions have been well-documented in other high-performance piezomaterials, usually in relation to a ground-state rhombohedral structure existing at low temperatures.[39−41] In the (111)-BTO film, a low-temperature rhombohedral structure was inferred from temperature-dependent Raman spectroscopy measurements,[6] but it has not been unambiguously demonstrated in other structural studies. Detailed investigation of the low-temperature crystal structure is highly desirable to enhance our understanding of the intriguing domain system of (111)-BTO film.

As in our previous work,[6] we investigated high-quality, 330 nm thick BTO films that were epitaxially grown on a (111)-STO substrate through pulsed laser deposition (PLD; Figure 1a) of an intermediate $SrRuO_3$ (SRO) layer to measure electrical properties. X-ray diffraction (XRD) and second-harmonic generation (SHG) analyses indicated that the BTO film at room temperature possesses a seemingly rhombohedral structure with an out-of-plane 3-fold rotational symmetry.[6] This is in contrast to the tetragonal structure of bulk BTO, as well as (001)-BTO films at room temperature. However, temperature-dependent dielectric spectra and Raman spectroscopy measurements suggest the existence of a structural transition at ∼220 K.[6] Although the rhombohedral structure is the lowest-energy ground state, in epitaxial films, the structural transition is usually complicated by the mechanical boundary condition.[42] In this context, it is vitally important to investigate the temperature-dependent structural transition and associated property changes of (111)-BTO film using in situ cryogenic STEM and optical measurements. Here, we will focus our discussions only on the mechanical boundary condition, without the electrostatic boundary condition as a governing parameter for the transitions. This is mostly because the latter is mostly considered prominent in ultrathin ferroelectric films (in the range of several nanometers) due to the finite size effect of the charge screening mechanism (see the supplementary discussions of the Supporting Information).[43,44]

We performed temperature-dependent electrical measurements. Figure 1a shows a detailed schematic of the capacitor geometry. Figure 1b shows the polarization−electric field (P−E) hysteresis loop of the (111)-BTO capacitor, which forms a slim, slanted P−E loop with small remnant polarization (P_r) at 300 K, suggesting a strong ferroelectric relaxation. As the temperature decreases (e.g., at 130 K), the P−E hysteresis loop becomes more square-shaped with increasing P_r. Figure 1c shows the evolution of P_r with temperature. In addition to the general trend of increasing P_r at lower temperature (see the supplementary discussions in the Supporting Information), the slope of increasing P_r changes at about 240 K. This observation supports the occurrence of an inferred phase transition around that temperature[6] and suggests that the low-temperature phase favors the out-of-plane polarization.

To elucidate this inferred phase transition, we performed temperature- and azimuth-dependent SHG measurements (Figure 1d). On the basis of the P-polarized incident wave, the P- and S-polarized SHG states were analyzed. Figure 1e shows representative SHG anisotropy patterns of the (111)-BTO film observed at 300 K. The P_{in}−P_{out} (PP) and P_{in}−S_{out} (PS) SHG patterns, which show 3- and 6-fold symmetry, are well-matched to the point group C_{3v}. As the temperature decreases to 90 K, the symmetry of each pattern remains unaltered, whereas the intensity of each contributing lobe changes slightly (Figure S3). To assess structural evolution according to the temperature, we compared the intensities of the major and minor lobes in the PP SHG anisotropy pattern. The ratio given by $I^{PP}_{Minor}(2\omega)/I^{PP}_{Major}(2\omega)$ (Figure 1f) tends to increase at the inferred transition temperature, similar to the change in P_r values shown in Figure 1c. On the basis of this information, we can estimate the structural evolution, although the macroscopic structural symmetry remains invariant.

To evaluate the change in the out-of-plane symmetry as a function of temperature, we compared the in-plane and out-of-plane nonlinear susceptibility components, i.e., a_1 and a_3, respectively (for details, see Figure S4). Figure 1f displays the temperature dependence of the a_3/a_1 ratio. In contrast to the aforementioned ratio of $I^{PP}_{Minor}(2\omega)/I^{PP}_{Major}(2\omega)$, the out-of-plane symmetric component increases as a_3/a_1 increases. During the initial cooling stage down to ∼240 K, a plateau was observed, followed by a clear increase. The turning point was coincident with the inferred phase transition temperature.[6] After the transition at ∼240 K, the ratio value continued to increase with decreasing temperature, that is, the out-of-plane symmetric components increased. These results are consistent with the afore discussed P−E hysteresis loop measurements, especially the plot of remnant polarization (Figure 1c). The observed SHG results reflect the average crystal symmetry of nanoscale domains because the probing beam spot size was set at 30 μm. Despite the fact that the macroscale crystal symmetry over a wide temperature range seems to be consistent with the rhombohedral phase, the actual local nanoscale crystalline structures could be different.

This intriguing phase transition with invariant macroscopic crystal symmetry was previously explained in terms of a transition from a polymorphic nanodomain state to a pure rhombohedral phase, based on phase-field simulations.[6] At room temperature, the (111)-BTO film possesses nanodomains of coexisting tetragonal, orthorhombic, and rhombohedral structures, and the averaged macroscopic response could resemble that of a rhombohedral structure. This is similar to the so-called adaptive phase at the morphotropic phase boundary of $PbZr_xTi_{1-x}O_3$, which exhibited a seemingly monoclinic structure in diffraction studies but actually consists of mixed tetragonal and rhombohedral nanodomains according to electron microscopy analyses.[45,46] To verify this possibility, we carried out STEM measurements.

The STEM images were obtained near the center regions of the film. The homogeneity of the (111)-BTO films in a broad thickness range (from ten to hundreds of nanometers) was previously proven by macroscopic characterization including PFM, P−E hysteresis loops, and XRD.[6] We further verified the homogeneity of the film as a function of depth using ultraviolet photoelectron spectroscopy (Figures S5). Therefore, the center region of our 330 nm thick BTO film might be able to represent the majority of the film well, despite the minor heterogeneity that could arise at the interfacial regions of the BTO film.

https://doi.org/10.1021/acs.nanolett.1c02729
Nano Lett. 2021, 21, 8679−8686

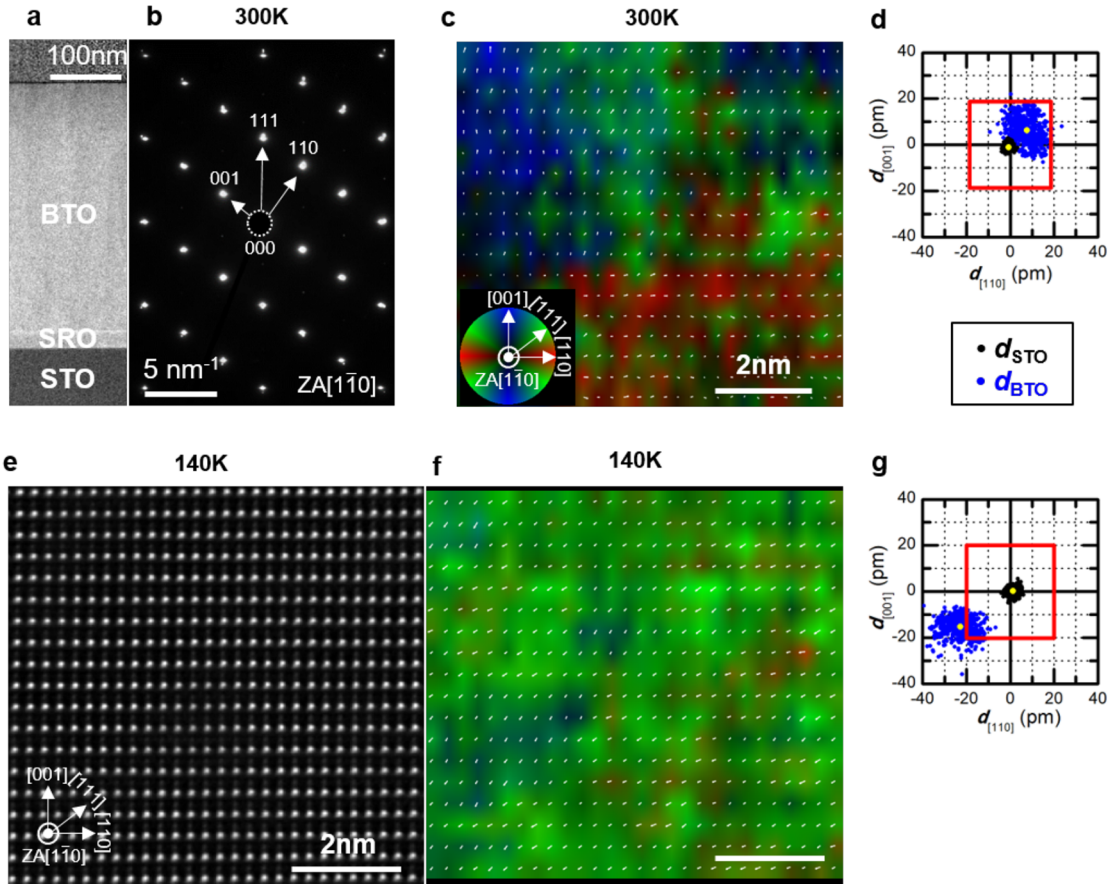

Figure 2. (a) Low-magnification HAADF-STEM image confirming a well-grown BTO film on (111)-STO with an intermediate SRO layer as a bottom electrode. (b) SAED pattern showing the epitaxial relationship of the BTO film with the SRO intermediate layer and STO substrate. The position of the direct electron beam is indicated by the white dotted circle. Crystal orientations are denoted by arrows with indexed reciprocal lattice points, which is shared with panel a. (c) 2D displacement vector map of the (111)-BTO film acquired from an atomic-resolution HAADF-STEM image at 300 K. Each vector was measured according to the relative displacement of Ti compared to the center of the Ba cage with picometer (pm)-precision. The field was drawn based on the color wheel (inset). (d) Ti-displacement vectors (blue) of (111)-BTO film are plotted in the vector space to show the vector distribution. The accuracy of the measurements is shown by the cluster of black dots representing the STO substrate around a value of 0 pm. The mean values of the two clusters are plotted as yellow dots. The red solid square represents the scanning pixel (px) size, which is 18.7 pm/px at 300 K. (e) HAADF-STEM image of (111)-BTO acquired at 140 K. (f) 2D displacement vector map drawn in accordance with the color wheel. (g) 2D displacement vector distributions of (111)-BTO (blue) and STO (black). The scanning step was 20.1 pm/px at 140 K. Using the two vector distributions, the polarization amplitude can be directly measured with variation in temperature. (Scale bar = 2 nm).

Figure 2a,b shows the low-magnification high-angle annular dark-field (HAADF)-STEM image and selected-area electron diffraction (SAED) pattern at 300 K, respectively. The BTO film is well-developed on STO, with an intermediate SRO layer as an electrode. Noticeably, the asymmetric reciprocal space mapping using X-ray revealed that the intermediate SRO layer is fully in-plane strained.[6] The SAED pattern also demonstrates an epitaxial relationship between the oxides. Figure 2a clearly shows both interfaces, STO/SRO and SRO/BTO. From the high-quality, atomic-resolution HAADF-STEM images of the BTO film, we mapped the Ti displacement vectors relative to the center of the nearest Ba-unit cage to directly visualize the domain structure. At 300 K, nanodomains with different symmetries were observed (Figure 2c), in agreement with the simulation results.[6] In Figure 2d, the corresponding distribution of Ti-displacement vectors in the space spanned by basis [110] and [001] are plotted with blue dots. These microscopic structural observations prove the formation of polymorphic nanodomains, though the averaged macroscopic response by SHG is similar to that of a rhombohedral structure which results in averaged [111]-polar state at 300 K. For comparison, Ti-displacement values of the STO substrate are plotted with black dots. The vanishing Ti displacements of STO, compared to those of BTO, demonstrate the accuracy and quality of our STEM images and data analysis technique. To quantitatively evaluate the reliability of STEM measurements at 300 K, we calculated the Ti-displacement vector cluster of STO using a Gaussian mixture model: $\mu_{[110]} = -0.6$ pm, $\mu_{[001]} = -0.9$ pm, $\sigma_{[110]} = 1.1$ pm, and $\sigma_{[001]} = 1.2$ pm, where μ and σ are the center and standard deviation of the Gaussian distribution, respectively. The directional information on the Cartesian coordinates is indicated by subscripts [110] and [001].

To obtain STEM images at lower temperature, we used a cryogenic liquid, i.e., liquid nitrogen, which typically causes serious experimental difficulties, including bubbling and vibrational drift (Figure S1). To overcome these difficulties, we acquired multiple images at fast scan speeds and applied postimage registration with a shift matrix.[25] Figure 2e shows a typical HAADF-STEM image of the (111)-BTO film at 140 K.

https://doi.org/10.1021/acs.nanolett.1c02729
Nano Lett. 2021, 21, 8679−8686

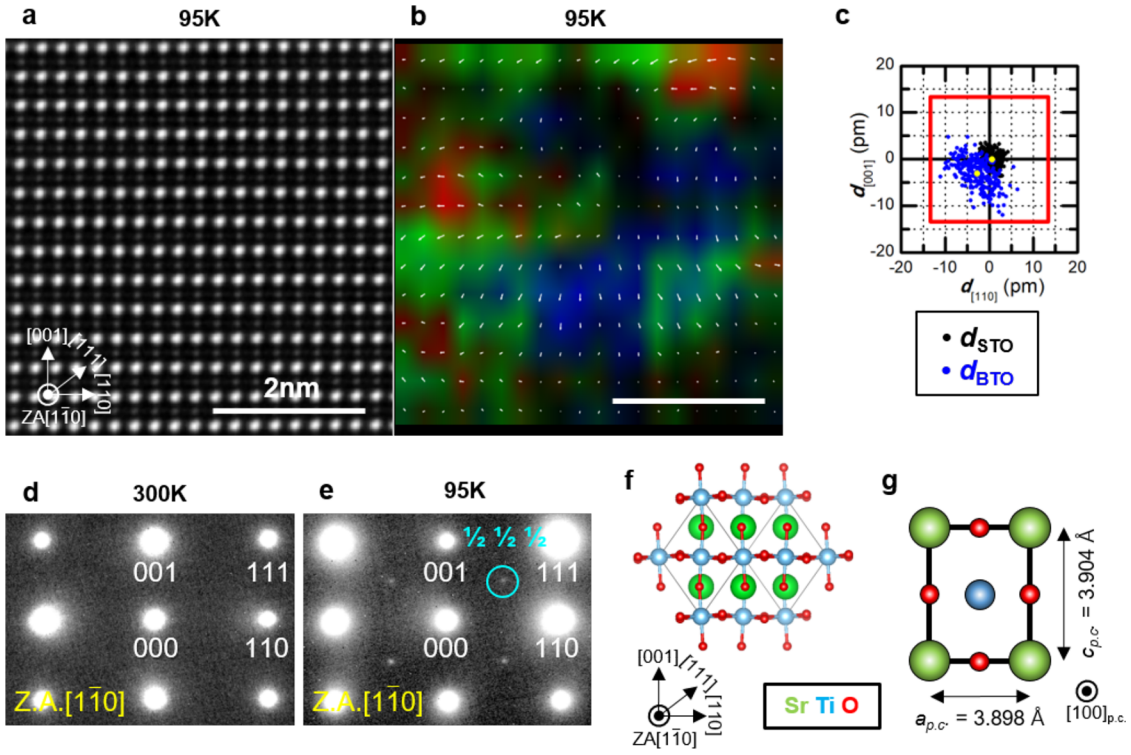

Figure 3. (a) HAADF-STEM image of (111)-BTO acquired at 95 K. (b) 2D displacement vector map was drawn based on the aforementioned color wheel. (c) 2D displacement vector distributions of (111)-BTO (blue) and STO (black). The scanning step was 13.4 pm/px at 95 K. (d) SAED pattern of the STO substrate at 300 K along the [1$\bar{1}$0] zone axis. (e) SAED pattern of the STO substrate at 95 K along the [1$\bar{1}$0] zone axis, showing extra spots (cyan circles) not visible at 300 K. (f) Illustration of the crystal structural model of STO with octahedral rotation ($a^0a^0c^-$) along the [1$\bar{1}$0] directions, corresponding to the axis vector reconstructed from unit-cell doubling and the SAED pattern at 95 K. (g) Exaggerative illustration of the pseudocubic-cell of tetragonal STO representing anisotropic elongation along $c_{p.c.}$ lattice viewing along $[100]_{p.c.}$ direction (scale bar = 2 nm).

This image is very high quality, reflected in the sharp contrast between the cation sublattices and dark background.

Using these high-quality images, we obtained the corresponding Ti-displacement map and distribution plot (Figure 2f,g, respectively). These images demonstrate that the (111)-BTO transforms into a pure rhombohedral phase at lower temperatures. Figure 2f clearly shows the pure rhombohedral phase of the BTO film with polarization in the [$\bar{1}\bar{1}\bar{1}$] direction, namely, toward the bottom electrode in the Figure 1a. This polarization state was seen in all of our STEM observations (Figure S6), except for one domain boundary observation (Figure S7). Compared to the phase-field simulations reported in our previous study,[6] these STEM results firmly establish that the rhombohedral phase is the low-temperature state of (111)-BTO. Moreover, Figure 2g shows stronger out-of-plane polarization than its 300 K counterpart (Figure 2d). The average [$\bar{1}\bar{1}\bar{1}$]-projected Ti displacement value is 27.4 pm at 140 K, which is much larger than that of 300 K (i.e., 9.9 pm). This difference explains the enhancement of P_r and SHG intensities at low temperatures. As for how domain evolution occurs during the transition, the phase-field simulations have shown that colossal rhombohedral domain emerges and grows while tetragonal and orthorhombic domains gradually disappear.[6]

Next, we evaluated the reliability of our low-temperature STEM measurements. Similar to the results obtained at 300 K (Figure 2d), the STO displacement vector was also calculated at 140 K. As shown in Figure 2g, we calculated the Ti-displacement vector cluster of STO at 140 K ($\mu_{[110]}$ = 1.3 pm, $\mu_{[001]}$ = 0.2 pm, $\sigma_{[110]}$ = 1.9 pm, and $\sigma_{[001]}$ = 1.5 pm). These Ti-displacement values of STO at 140 K are much smaller than those of BTO, and comparable to those of STO at 300 K, indicating that reliable high-quality STEM images can be obtained using cryogenic experiments.

We further lowered the measurement temperature to 95 K, which is the lowest temperature we can reach. Though the STEM specimen stage was cooled down by LN_2, the sample could not reach LN_2 temperature (77 K) due to thermal loss of thermal conductor consisting TEM holder. Interestingly, we observed that the single rhombohedral domain collapsed into complex nanodomains. Figure 3a,b displays a fine atomic-resolution STEM image and the corresponding Ti-displacement vector map of BTO at 95 K, respectively. Figure 3c displays the corresponding distribution plot of Ti-displacement vectors of the STO substrate (black) and BTO film (blue). The Ti-distribution values of STO are quite small ($\mu_{[110]}$ = 0.7 pm, $\mu_{[001]}$ = −0.1 pm, $\sigma_{[110]}$ = 1.3 pm, and $\sigma_{[001]}$ = 1.5 pm), again demonstrating the reliability of our measurements. In contrast, the Ti-displacement vector map for the BTO shows a complex polarization pattern with significant rotation at the nanoscale (Figure 3b). The magnitude of the polarization decreased sharply with a dispersed distribution of polar directions (Figure 3c). The emergence of complex nanodomains was unexpected, given that bulk BTO exhibits no structural phase transition at temperatures below 183 K.

This unexpected state is likely attributable to the mechanical constraints on the STO substrate at 95 K. It is known that cubic STO undergoes a structural phase transition into the

https://doi.org/10.1021/acs.nanolett.1c02729
Nano Lett. 2021, 21, 8679−8686

tetragonal phase having a cationic distortion of *c*-axis lengthening at 105 K.[17] This transition is supported by SAED measurements of the STO substrate at 300 and 95 K (Figure 3d,e, respectively) because it is accompanied by oxygen octahedral rotations (OOR) of $a^0a^0c^-$ pattern system in Glazer notation (Figure 3f).[17,47,48] The half-integer diffraction spots emerge between the first-order reciprocal peaks due to cell-doubling by OOR. However, OOR is not a driving way of symmetry breakdown because it is known that OOR connectivity is confined within only a few unit cells.[49−51] To clarify this issue, we obtained SAED patterns of BTO covering STEM observation area by temperature (Figure S8). The fact that no extra spots emerges at 95 K confirmed that BTO has no OOR. Instead, the asymmetric lattice parameters ($a_{p.c.}$ = 3.898 Å and $c_{p.c.}$ = 3.904 Å)[52] of tetragonal STO regarding cationic sublattices play a key role as a mechanical boundary perturbation below 105 K, namely, the break down of 3-fold rotational symmetry along out-of-plane direction (Figure 3g). Tetragonal cationic cell-cage generates anisotropic strains in the in-plane dimension, which lead to the transformation into the polymorphic nanodomains.[53] This second-stage spontaneous transition of ferroelectric domains was also verified by the afore discussed SHG measurements. As shown in Figure 1f, we observed an additional slope change below 105 K in the plots of both ratios, $I^{PP}_{Minor}(2\omega)/I^{PP}_{Major}(2\omega)$ and a_3/a_1, followed by an increasing and decreasing trend, respectively. The slope change after the transition indicates that the ferroelectric domain structure collapsed again into complex nanodomains. Notably, despite the structural similarities between the nanodomain structure below 105 K and that at room temperature, the (111)-BTO film exhibits large remnant polarization, i.e., negligible polar relaxation, from the *P*−*E* response below 105 K (Figure 1b,c). These behaviors can be explained by suppressed thermal fluctuations at low temperatures. In the previous study, the phase-field simulation showed that the polarization in our 330 nm thick (111)-BTO film is easily reoriented toward the direction of the applied out-of-plane electric field, thus resulting in massive transition to [111]-polarized rhombohedral phase even at 300 K.[6] However, at 300 K, our ferroelectric films exhibited strong polarization relaxation, where the thermal fluctuation is responsible as in the case of conventional relaxor ferroelectrics.[6,54,55] Therefore, the thermal energy could disrupt the field-driven electric dipole alignments, resulting in polarization relaxation and small remnant polarization. In contrast, the cryogenic environment significantly reduces the thermal energy, thus, makes the stable ferroelectric state, just as the conventional relaxor ferroelectrics form long-range ferroelectric domains resulting in ferroelectric transition. In other words, ferroelectric transition from the relaxor ferroelectric state represents itself such that the thermal activation is significantly suppressed. Therefore, electric-field-aligned electric dipoles along the out-of-plane direction maintain an unstirred remnant polarization at appreciably low temperatures, thereby resulting in the discussing discrepancy.

This work demonstrated the critical role of substrate clapping effects in ferroelectric domain formation. On the basis of high-precision in situ cryogenic observation over the entire phase transition range, we showed that ferroelectric BTO film grown on (111)-STO undergoes a two-stage phase transition, accompanied by both mechanical clamping and thermodynamic driving forces. These observations show that the structural transition of the substrate must be taken into account when interpreting the physical properties of thin film systems, constrained by the nature of the substrate surface symmetry.

In conclusion, we report direct observation of thermally driven phase transitions of (111)-BTO film at the atomic level under the influence of substrate clamping, particularly with symmetry enforcement. A correlation between the phase transition and electrical properties was also identified. Two-stage phase transitions of the (111)-BTO film occurred as the temperature was lowered over the range from 300 to 95 K. In the first stage, ferroelectricity was enhanced, as evidenced by the increased domain size and polarization magnitude of the [111]-polarized ground rhombohedral phase BTO. In the following stage, antiferrodistortion of the STO substrate caused a symmetric mismatch between the ground polarization direction of BTO and the substrate surface, resulting in the formation of mixed-state polarization domains. Our results provide new insight that could facilitate further development of functional materials, e.g., through manipulating the morphotropic boundary in a variety of heterostructures using substrates with thermal expansion coefficient mismatch. Furthermore, the accuracy of the atomic-level cryogenic electron microscopy measurements provides direct evidence of local microstructural changes, such as chemical inhomogeneity and structural variations, which affect macroscopic properties. Combined with SHG analysis, the changes in crystal structure with temperature are comprehensively understood from macro and microscopic perspectives. This capability has immense potential for explaining structure−property relationships in numerous functional materials.

■ ASSOCIATED CONTENT

Supporting Information

The Supporting Information is available free of charge at https://pubs.acs.org/doi/10.1021/acs.nanolett.1c02729.

Experimental/computational methods; discussions on boundary conditions and remnant polarization results by temperature; additional cryogenic HAADF STEM images and SAED patterns; all temperature- and azimuth-dependent SHG patterns (PDF)

■ AUTHOR INFORMATION

Corresponding Author

Miyoung Kim − *Center for Correlated Electron Systems, Institute for Basic Science (IBS), Seoul 08826, Republic of Korea; Department of Materials Science and Engineering and Research Institute of Advanced Materials, Seoul National University, Seoul 08826, Republic of Korea;* orcid.org/0000-0001-8632-6711; Email: mkim@snu.ac.kr

Authors

Junsik Mun − *Center for Correlated Electron Systems, Institute for Basic Science (IBS), Seoul 08826, Republic of Korea; Department of Materials Science and Engineering and Research Institute of Advanced Materials, Seoul National University, Seoul 08826, Republic of Korea*

Wei Peng − *Center for Correlated Electron Systems, Institute for Basic Science (IBS), Seoul 08826, Republic of Korea; Department of Physics and Astronomy, Seoul National University, Seoul 08826, Republic of Korea*

Chang Jae Roh − *Center for Correlated Electron Systems, Institute for Basic Science (IBS), Seoul 08826, Republic of*

Korea; Department of Physics and Astronomy, Seoul National University, Seoul 08826, Republic of Korea; Department of Physics and Photon Science, Gwangju Institute of Science and Technology, Gwangju 61005, Republic of Korea

Sangmin Lee − *Center for Correlated Electron Systems, Institute for Basic Science (IBS), Seoul 08826, Republic of Korea; Department of Materials Science and Engineering and Research Institute of Advanced Materials, Seoul National University, Seoul 08826, Republic of Korea*

Syo Matsumura − *Department of Applied Quantum Physics and Nuclear Engineering, Kyushu University, Fukuoka 819-0395, Japan*

Jong Seok Lee − *Department of Physics and Photon Science, Gwangju Institute of Science and Technology, Gwangju 61005, Republic of Korea;* orcid.org/0000-0001-6317-7944

Tae Won Noh − *Center for Correlated Electron Systems, Institute for Basic Science (IBS), Seoul 08826, Republic of Korea; Department of Physics and Astronomy, Seoul National University, Seoul 08826, Republic of Korea;* orcid.org/0000-0003-1905-2321

Complete contact information is available at: https://pubs.acs.org/10.1021/acs.nanolett.1c02729

Author Contributions

The manuscript was written through contributions of all authors. All authors have given approval to the final version of the manuscript.

Notes

The authors declare no competing financial interest.

■ ACKNOWLEDGMENTS

This work was supported by the Research Center Program of IBS (Institute for Basic Science) in Korea (IBS-R009-D1), National Research Foundation of Korea (NRF) grant funded by the Korea government (MSIT) (NRF-2017R1A2B3011629), the Ministry of Science, ICT, and Future Planning (MSIP) (Nos. 2015R1A5A1009962). STEM measurements were supported by the National Center for Inter-University Research Facilities (NCIRF) at Seoul National University in Korea and MEXT Advanced Characterization Nanotechnology Platform (JPMXP09A19KU0299) in Japan.

■ REFERENCES

(1) Lines, M. E.; Glass, A. M. Principles and Applications of Ferroelectrics and Related Materials. *OUP Oxford* **2001**, 1−680.

(2) Cross, L. E. Ferroelectric Ceramics: Tailoring Properties for Specific Applications. In *Ferroelectric Ceramics*; Setter, N., Colla, E. L., Eds.; Birkhäuser Basel, 1993; pp 1−85.

(3) Zeches, R. J.; Rossell, M. D.; Zhang, J. X.; Hatt, A. J.; He, Q.; Yang, C. H.; Kumar, A.; Wang, C. H.; Melville, A.; Adamo, C.; Sheng, G.; Chu, Y. H.; Ihlefeld, J. F.; Erni, R.; Ederer, C.; Gopalan, V.; Chen, L. Q.; Schlom, D. G.; Spaldin, N. A.; Martin, L. W.; Ramesh, R. A Strain-Driven Morphotropic Phase Boundary in $BiFeO_3$. *Science* **2009**, *326*, 977−980.

(4) Ahart, M.; Somayazulu, M.; Cohen, R. E.; Ganesh, P.; Dera, P.; Mao, H. K.; Hemley, R. J.; Ren, Y.; Liermann, P.; Wu, Z. G. Origin of morphotropic phase boundaries in ferroelectrics. *Nature* **2008**, *451*, 545−548.

(5) Saito, Y.; Takao, H.; Tani, T.; Nonoyama, T.; Takatori, K.; Homma, T.; Nagaya, T.; Nakamura, M. Lead-free piezoceramics. *Nature* **2004**, *432*, 84−87.

(6) Peng, W.; Zorn, J. A.; Mun, J.; Sheeraz, M.; Roh, C. J.; Pan, J.; Wang, B.; Guo, K.; Ahn, C. W.; Zhang, Y. P.; Yao, K.; Lee, J. S.; Chung, J. S.; Kim, T. H.; Chen, L. Q.; Kim, M.; Wang, L. F.; Noh, T. W. Constructing Polymorphic Nanodomains in $BaTiO_3$ Films via Epitaxial Symmetry Engineering. *Adv. Funct. Mater.* **2020**, *30*, 1910569.

(7) Jin, Y. M.; Wang, Y. U.; Khachaturyan, A. G.; Li, J. F.; Viehland, D. J. Adaptive ferroelectric states in systems with low domain wall energy: Tetragonal microdomains. *J. Appl. Phys.* **2003**, *94*, 3629−3640.

(8) Rossetti, G. A.; Khachaturyan, A. G. Inherent nanoscale structural instabilities near morphotropic boundaries in ferroelectric solid solutions. *Appl. Phys. Lett.* **2007**, *91*, 072909.

(9) Yadav, A.; Nelson, C.; Hsu, S.; Hong, Z.; Clarkson, J.; Schlepütz, C.; Damodaran, A.; Shafer, P.; Arenholz, E.; Dedon, L.; et al. Observation of polar vortices in oxide superlattices. *Nature* **2016**, *530*, 198−201.

(10) Das, S.; Tang, Y.; Hong, Z.; Gonçalves, M.; McCarter, M.; Klewe, C.; Nguyen, K.; Gómez-Ortiz, F.; Shafer, P.; Arenholz, E. Observation of room-temperature polar skyrmions. *Nature* **2019**, *568*, 368−372.

(11) Li, L. Z.; Cheng, X. X.; Jokisaari, J. R.; Gao, P.; Britson, J.; Adamo, C.; Heikes, C.; Schlom, D. G.; Chen, L. Q.; Pan, X. Q. Defect-Induced Hedgehog Polarization States in Multiferroics. *Phys. Rev. Lett.* **2018**, *120*, 137602.

(12) Sun, C. T.; Achuthan, A. Domain-switching criteria for ferroelectric materials subjected to electrical and mechanical loads. *J. Am. Ceram. Soc.* **2004**, *87*, 395−400.

(13) Chen, Z. B.; Hong, L.; Wang, F. F.; Ringer, S. P.; Chen, L. Q.; Luo, H. S.; Liao, X. Z. Facilitation of Ferroelectric Switching via Mechanical Manipulation of Hierarchical Nanoscale Domain Structures. *Phys. Rev. Lett.* **2017**, *118*, 017601.

(14) Chang, H. J.; Kalinin, S. V.; Yang, S.; Yu, P.; Bhattacharya, S.; Wu, P. P.; Balke, N.; Jesse, S.; Chen, L. Q.; Ramesh, R.; Pennycook, S. J.; Borisevich, A. Y. Watching domains grow: In situ studies of polarization switching by combined scanning probe and scanning transmission electron microscopy. *J. Appl. Phys.* **2011**, *110*, 052014.

(15) Du, K.; Zhang, M.; Dai, C.; Zhou, Z. N.; Xie, Y. W.; Ren, Z. H.; Tian, H.; Chen, L. Q.; Van Tendeloo, G.; Zhang, Z. Manipulating topological transformations of polar structures through real-time observation of the dynamic polarization evolution. *Nat. Commun.* **2019**, *10*, 4864.

(16) Chen, P.; Zhong, X.; Zorn, J. A.; Li, M.; Sun, Y.; Abid, A. Y.; Ren, C.; Li, Y.; Li, X.; Ma, X.; et al. Atomic imaging of mechanically induced topological transition of ferroelectric vortices. *Nat. Commun.* **2020**, *11*, 1840.

(17) Tsuda, K.; Tanaka, M. Refinement of Crystal-Structure Parameters Using Convergent-Beam Electron Diffraction: the Low-Temperature Phase of $SrTiO_3$. *Acta Crystallogr., Sect. A: Found. Crystallogr.* **1995**, *51*, 7−19.

(18) Sun, W.; Kimoto, T.; Furubayashi, T.; Matsumoto, T.; Ikeda, S.; Nagata, S. In-situ low-temperature transmission electron microscopy of the structural phase transitions in a thiospinel $CuIr_2S_4$ compound. *J. Phys. Soc. Jpn.* **2001**, *70*, 2817−2820.

(19) Tsuda, K.; Sano, R.; Tanaka, M. Nanoscale local structures of rhombohedral symmetry in the orthorhombic and tetragonal phases of $BaTiO_3$ studied by convergent-beam electron diffraction. *Phys. Rev. B: Condens. Matter Mater. Phys.* **2012**, *86*, 214106.

(20) Sang, X. H.; LeBeau, J. M. Revolving scanning transmission electron microscopy: Correcting sample drift distortion without prior knowledge. *Ultramicroscopy* **2014**, *138*, 28−35.

(21) Berkels, B.; Binev, P.; Blom, D. A.; Dahmen, W.; Sharpley, R. C.; Vogt, T. Optimized imaging using non-rigid registration. *Ultramicroscopy* **2014**, *138*, 46−56.

(22) Ophus, C.; Ciston, J.; Nelson, C. T. Correcting nonlinear drift distortion of scanning probe and scanning transmission electron microscopies from image pairs with orthogonal scan directions. *Ultramicroscopy* **2016**, *162*, 1−9.

(23) Ning, S. C.; Fujita, T.; Nie, A. M.; Wang, Z. Q.; Xu, X. D.; Chen, J. H.; Chen, M. W.; Yao, S. H.; Zhang, T. Y. Scanning distortion correction in STEM images. *Ultramicroscopy* **2018**, *184*, 274−283.
(24) Wang, Y.; Suyolcu, Y. E.; Salzberger, U.; Hahn, K.; Srot, V.; Sigle, W.; van Aken, P. A. Correcting the linear and nonlinear distortions for atomically resolved STEM spectrum and diffraction imaging. *Microscopy* **2018**, *67*, i114−i122.
(25) Savitzky, B. H.; El Baggari, I.; Clement, C. B.; Waite, E.; Goodge, B. H.; Baek, D. J.; Sheckelton, J. P.; Pasco, C.; Nair, H.; Schreiber, N. J. Image registration of low signal-to-noise cryo-STEM data. *Ultramicroscopy* **2018**, *191*, 56−65.
(26) El Baggari, I.; Savitzky, B. H.; Admasu, A. S.; Kim, J.; Cheong, S. W.; Hovden, R.; Kourkoutis, L. F. Nature and evolution of incommensurate charge order in manganites visualized with cryogenic scanning transmission electron microscopy. *Proc. Natl. Acad. Sci. U. S. A.* **2018**, *115*, 1445−1450.
(27) El Baggari, I.; Baek, D. J.; Zachman, M. J.; Lu, D.; Hikita, Y.; Hwang, H. Y.; Nowadnick, E. A.; Kourkoutis, L. F. Charge order textures induced by non-linear couplings in a half-doped Manganite. *Nat. Commun.* **2021**, *12*, 3747.
(28) El Baggari, I.; Sivadas, N.; Stiehl, G. M.; Waelder, J.; Ralph, D. C.; Fennie, C. J.; Kourkoutis, L. F. Direct Visualization of Trimerized States in 1T′-$TaTe_2$. *Phys. Rev. Lett.* **2020**, *125*, 165302.
(29) Megaw, H. D. Crystal Structure of Barium Titanate. *Nature* **1945**, *155*, 484−485.
(30) Miyake, S.; Ueda, R. On Polymorphic Change of $BaTiO_3$. *J. Phys. Soc. Jpn.* **1946**, *1*, 32−33.
(31) Kay, H. F.; Vousden, P. Symmetry Changes in Barium Titanate at Low Temperatures and Their Relation to Its Ferroelectric Properties. *Philos. Mag.* **1949**, *40*, 1019−1040.
(32) Abrahams, S. C.; Kurtz, S. K.; Jamieson, P. B. Atomic Displacement Relationship to Curie Temperature and Spontaneous Polarization in Displacive Ferroelectrics. *Phys. Rev.* **1968**, *172*, 551.
(33) Jia, C. L.; Nagarajan, V.; He, J. Q.; Houben, L.; Zhao, T.; Ramesh, R.; Urban, K.; Waser, R. Unit-cell scale mapping of ferroelectricity and tetragonality in epitaxial ultrathin ferroelectric films. *Nat. Mater.* **2007**, *6*, 64−69.
(34) Chisholm, M. F.; Luo, W. D.; Oxley, M. P.; Pantelides, S. T.; Lee, H. N. Atomic-Scale Compensation Phenomena at Polar Interfaces. *Phys. Rev. Lett.* **2010**, *105*, 197602.
(35) Yadav, A. K.; Nelson, C. T.; Hsu, S. L.; Hong, Z.; Clarkson, J. D.; Schleputz, C. M.; Damodaran, A. R.; Shafer, P.; Arenholz, E.; Dedon, L. R.; Chen, D.; Vishwanath, A.; Minor, A. M.; Chen, L. Q.; Scott, J. F.; Martin, L. W.; Ramesh, R. Observation of polar vortices in oxide superlattices. *Nature* **2016**, *534*, 138−138.
(36) Bokov, A. A.; Ye, Z. G. Recent progress in relaxor ferroelectrics with perovskite structure. *J. Mater. Sci.* **2006**, *41*, 31−52.
(37) Wada, S.; Suzuki, S.; Noma, T.; Suzuki, T.; Osada, M.; Kakihana, M.; Park, S. E.; Cross, L. E.; Shrout, T. R. Enhanced piezoelectric property of barium titanate single crystals with engineered domain configurations. *Jpn. J. Appl. Phys.* **1999**, *38*, 5505−5511.
(38) Brajesh, K.; Tanwar, K.; Abebe, M.; Ranjan, R. Relaxor ferroelectricity and electric-field-driven structural transformation in the giant lead-free piezoelectric (Ba,Ca)(Ti, Zr)O_3. *Phys. Rev. B: Condens. Matter Mater. Phys.* **2015**, *92*, 224112.
(39) Noheda, B.; Cox, D. E.; Shirane, G.; Gonzalo, J. A.; Cross, L. E.; Park, S. E. A monoclinic ferroelectric phase in the $Pb(Zr_{1-x}Ti_x)O_3$ solid solution. *Appl. Phys. Lett.* **1999**, *74*, 2059−2061.
(40) Zhang, J. X.; Xiang, B.; He, Q.; Seidel, J.; Zeches, R. J.; Yu, P.; Yang, S. Y.; Wang, C. H.; Chu, Y. H.; Martin, L. W.; Minor, A. M.; Ramesh, R. Large field-induced strains in a lead-free piezoelectric material. *Nat. Nanotechnol.* **2011**, *6*, 98−102.
(41) Li, F.; Zhang, S. J.; Yang, T. N.; Xu, Z.; Zhang, N.; Liu, G.; Wang, J. J.; Wang, J. L.; Cheng, Z. X.; Ye, Z. G.; et al. The origin of ultrahigh piezoelectricity in relaxor-ferroelectric solid solution crystals. *Nat. Commun.* **2016**, *7*, 13807.
(42) Damodaran, A. R.; Agar, J. C.; Pandya, S.; Chen, Z. H.; Dedon, L.; Xu, R. J.; Apgar, B.; Saremi, S.; Martin, L. W. New modalities of strain-control of ferroelectric thin films. *J. Phys.: Condens. Matter* **2016**, *28*, 263001.
(43) Kretschmer, R.; Binder, K. Surface Effects on Phase-Transitions in Ferroelectrics and Dipolar Magnets. *Phys. Rev. B: Condens. Matter Mater. Phys.* **1979**, *20*, 1065−1076.
(44) Eliseev, E. A.; Kalinin, S. V.; Morozovska, A. N. Finite size effects in ferroelectric-semiconductor thin films under open-circuit electric boundary conditions. *J. Appl. Phys.* **2015**, *117*, 034102.
(45) Cao, W. W.; Cross, L. E. Theoretical-Model for the Morphotropic Phase-Boundary in Lead Zirconate Lead Titanate Solid-Solution. *Phys. Rev. B: Condens. Matter Mater. Phys.* **1993**, *47*, 4825−4830.
(46) Theissmann, R.; Schmitt, L. A.; Kling, J.; Schierholz, R.; Schonau, K. A.; Fuess, H.; Knapp, M.; Kungl, H.; Hoffmann, M. J. Nanodomains in morphotropic lead zirconate titanate ceramics: On the origin of the strong piezoelectric effect. *J. Appl. Phys.* **2007**, *102*, 024111.
(47) Riste, T.; Samuelsen, E. J.; Otnes, K.; Feder, J. Critical Behaviour of $SrTiO_3$ near 105 Degrees Phase Transition. *Solid State Commun.* **1971**, *9*, 1455−1458.
(48) Glazer, A. The classification of tilted octahedra in perovskites. *Acta Crystallogr., Sect. B: Struct. Crystallogr. Cryst. Chem.* **1972**, *28*, 3384−3392.
(49) May, S. J.; Kim, J. W.; Rondinelli, J. M.; Karapetrova, E.; Spaldin, N. A.; Bhattacharya, A.; Ryan, P. J. Quantifying octahedral rotations in strained perovskite oxide films. *Phys. Rev. B: Condens. Matter Mater. Phys.* **2010**, *82*, 014110.
(50) Borisevich, A. Y.; Chang, H. J.; Huijben, M.; Oxley, M. P.; Okamoto, S.; Niranjan, M. K.; Burton, J. D.; Tsymbal, E. Y.; Chu, Y. H.; Yu, P.; Ramesh, R.; Kalinin, S. V.; Pennycook, S. J. Suppression of Octahedral Tilts and Associated Changes in Electronic Properties at Epitaxial Oxide Heterostructure Interfaces. *Phys. Rev. Lett.* **2010**, *105*, 087204.
(51) Chang, S. H.; Chang, Y. J.; Jang, S. Y.; Jeong, D. W.; Jung, C. U.; Kim, Y. J.; Chung, J. S.; Noh, T. W. Thickness-dependent structural phase transition of strained $SrRuO_3$ ultrathin films: The role of octahedral tilt. *Phys. Rev. B: Condens. Matter Mater. Phys.* **2011**, *84*, 104101.
(52) Kiat, J. M.; Roisnel, T. Rietveld analysis of strontium titanate in the Muller state. *J. Phys.: Condens. Matter* **1996**, *8*, 3471−3475.
(53) Sheng, G.; Zhang, J. X.; Li, Y. L.; Choudhury, S.; Jia, Q. X.; Liu, Z. K.; Chen, L. Q. Misfit strain−misfit strain diagram of epitaxial $BaTiO_3$ thin films: Thermodynamic calculations and phase-field simulations. *Appl. Phys. Lett.* **2008**, *93*, 232904.
(54) Fu, D. S.; Taniguchi, H.; Itoh, M.; Koshihara, S.; Yamamoto, N.; Mori, S. Relaxor $Pb(Mg_{1/3}Nb_{2/3})O_3$: A Ferroelectric with Multiple Inhomogeneities. *Phys. Rev. Lett.* **2009**, *103*, 207601.
(55) Hu, Q. Y.; Wei, X. Y. Abnormal phase transition and polarization mismatch phenomena in $BaTiO_3$-based relaxor ferroelectrics. *J. Adv. Dielectr.* **2019**, *9*, 1930002.

https://doi.org/10.1021/acs.nanolett.1c02729
Nano Lett. 2021, 21, 8679−8686